

Radio-frequency coils for ultra-high field magnetic resonance



Özlem Ipek, PhD

CIBM-AIT, École Polytechnique Fédérale de Lausanne (EPFL), Lausanne, Switzerland

ARTICLE INFO

Article history:

Received 3 August 2016

Received in revised form

24 March 2017

Accepted 27 March 2017

Available online 29 March 2017

Keywords:

Magnetic resonance

Radiofrequency (RF) coils

Ultra-high field MR

Specific absorption rate (SAR)

Electromagnetic field simulation

Transmit field (B_1^+)

ABSTRACT

Radiofrequency (RF) coils are key components of magnetic resonance imaging (MRI) systems. The primary purpose of this review is to provide a basic theory of RF coil designs and their characterization by bench measurements, electromagnetic field simulations and MR measurements. With the continuing increase of magnetic field strength in MRI instruments, the RF wavelength in the subject under study becomes comparable to or smaller in size than the anatomical dimensions of the tissue under study, which amplifies the signal inhomogeneity. Also, RF energy increases quadratically with the Larmor frequency, which leads to increased heat deposition in the subject, especially at ultra-high field. Elegant RF coil designs are explored here to address these challenges.

© 2017 Elsevier Inc. All rights reserved.

Introduction

Radiofrequency (RF) coils on magnetic resonance (MR) scanners are used for transmitting and receiving the RF signal at a single frequency. An RF pulse is applied for duration of micro-to milliseconds in order to tip the magnetization from its equilibrium position. A high-power RF pulse (typically in the kW range) with a constant amplitude and phase induces a current in the coil conductor. On the receive side, oscillations of the magnetic field due to the resonating spins induce a voltage in a coil conductor. In contrast to the transmit signal, the receive signal is at much lower power. Therefore, before the (millivolt-level) signal is digitized with an analog-to-digital (A/D) converter, it is first amplified by low-noise preamplifiers. Moreover, sufficient isolation of the signal transmission from the signal reception is important to protect the MR system's sensitive receive electronics. A transmit/receive switch and active receive blanking are used to ensure that the transmission reception signal leakage is minimized. Therefore, the transmit/receive switch must have high power capacity (4–16 kW for 7 T), fast switching (<10 μ s), and high isolation between the two channels (>30 dB) [1].

An RF coil consists essentially of an inductor and a capacitor, known as lumped elements. A capacitor can be connected in parallel and in series for tuning to the appropriate/desired frequency, and for matching to 50 Ohms (Ω), which is the termination for all MR electronics, respectively (Fig. 1a) [2]. The coil components must be non-magnetic and be able to handle a high RF power input. In

general, as a conductor, copper wire, copper tape or silver plated wires can be utilized with non-magnetic parallel-plate ceramic capacitors or ceramic trimmer (variable, i.e. 1 to 10 pF range) capacitors, non-magnetic inductors, or varnished copper wires used as an inductor with non-magnetic connectors and coaxial cables at 50 Ω . As an alternative to rigid copper wires, feasibility studies of flexible RF coils using inkjet- [3] and screen- [4] printed conductors have been reported. The components should be arranged symmetrically with respect to ground to ensure a zero voltage relative to the rest of the coil. Maximum conductor length should be smaller than wavelength/20 to avoid a standing wave between lumped elements and source [2]. This can be achieved by distributing the capacitors around the coil.

The RF coil must be tuned at the nuclei Larmor frequency and matched to 50 Ω to transmit the maximum input RF power into the imaging subject (Fig. 2). By varying the inductor (in the nH range) and capacitor (in the pF range) values, the reflection coefficient of the RF circuit with respect to the 50 Ω transmission line can be minimized to -13 dB or better. This ensures that the reflected power is minimized to 5% of the input RF power. As the resistance in the circuit increases, the quality of the resonance will be reduced. The sharpness of the resonance peak is described by the quality factor (Q -factor) which is defined as the resonance frequency divided by the full-width-half-maximum bandwidth. Upon loading of the RF coil with a subject or sample, the Q -factor should drop. If the ratio of the unloaded to loaded Q -factor is 6, the power loss in the imaged subject is 5-fold greater than the losses in the coil

List of abbreviations

RF	Radiofrequency	SAR	Specific absorption rate
kW	kiloWatt	IEC	International Electrotechnical Commission
A/D	Analog-to-Digital	VOPs	Virtual observation points
T	Tesla	Hz	Hertz
dB	Decibel	CEM43	Cumulative Equivalent Minutes at 43 °C
F	Farad	EM	Electromagnetic
H	Henry	CAD	Computer-Aided Design
Q-factor	Quality factor	PEC	Perfect Electric Conductor
S	Siemens	FDTD	Finite-Difference Time-Domain
FOV	Field-of-view	FEM/FIM	Finite Element/Integration Method
SNR	Signal-to-noise ratio	B ₁ ⁺ map	RF field mapping
BOLD	Blood-Oxygen-Level Dependent	SA2RAGE	Saturation prepared with 2 Rapid Gradient Echoes
fMRI	Functional MRI	DREAM	Dual Refocusing Echo Acquisition Method
		CSF	Cerebrospinal fluid
		VNA	Vector network analyzer

components. A low Q-factor may indicate high loss or a large frequency bandwidth.

To mimic the human brain as an imaging subject, a sphere-shaped homogeneous phantom filled with tissue-simulating liquid or gel can be utilized. A phantom with the same dielectric properties as typical brain tissue can be utilized to test the RF coils on the bench and on the MR scanner. For example, the average dielectric constant of the human brain is 55 and electrical conductivity is 0.7 S/m at 300 MHz (7 T). The main ingredient of the phantom is water, which has a dielectric constant of 80 at 300 MHz. Salt (NaCl) can be added to increase the electrical conductivity, while table sugar is used to decrease the dielectric constant. But added sugar leads to a poor quality MR signal. Therefore, polyethylene-based chemicals are preferred along with agar mixtures to decrease the dielectric constant [5].

The main categories of RF coils are volume and surface coils (Fig. 3). As volume coils permit imaging of a larger field-of-view (FOV) with a homogeneous excitation, surface coils provide high efficiency and sensitivity in the vicinity of the coil. Surface coils are mainly used as a receive coil array, as they are characterized (in addition to their high receive sensitivity in the vicinity of the coil) by a low noise pick up as they couple to a limited tissue volume [6]. Coupling between the array elements leads to resonance peak splitting and reduced transmit efficiency as a result of the conducting current leaking into the neighboring array element.

Adjacent surface coil elements [7] can be partially overlapped to cancel the mutual inductance. For the array elements, cable routing must be fixed to minimize the cable-to-cable coupling as well as cable-to-electronics coupling on the scanner/patient bed.

RF coils can be used as transceivers, independent transmit or receive coils and as double-tuned coils. The same RF coil transmits and receives the RF signal as a transceiver, while separate RF coil designs are utilized as independent transmit and receive. For example, the commercial 7T head coil manufactured by Nova Medical (Wilmington, MA) consists of a single-channel birdcage transmit coil and 32-channel surface loop receive coils. The advantage of the multi-channel receive array is to increase the local sensitivity in the peripheral part of the brain where the transmit field is low (Fig. 6a). This results in enhanced homogeneity in overall MR signal for conventional gradient echo imaging despite unwanted image contrast changes due to the variations in the transmit field distribution. This also improves the acquisition speed by using parallel imaging methods. Furthermore, multi-nuclei (e.g. ¹³C, ¹⁵N, ³¹P) MR imaging/spectroscopy requires single/multiple RF coils tuned to multiple frequencies. For example, a combination of a linear phosphorous and quadrature proton RF loop coils (Fig. 1b) can be used for the acquisition of high quality ³¹P spectra in the occipital lobe of the human brain and for proton signal localization and shimming.

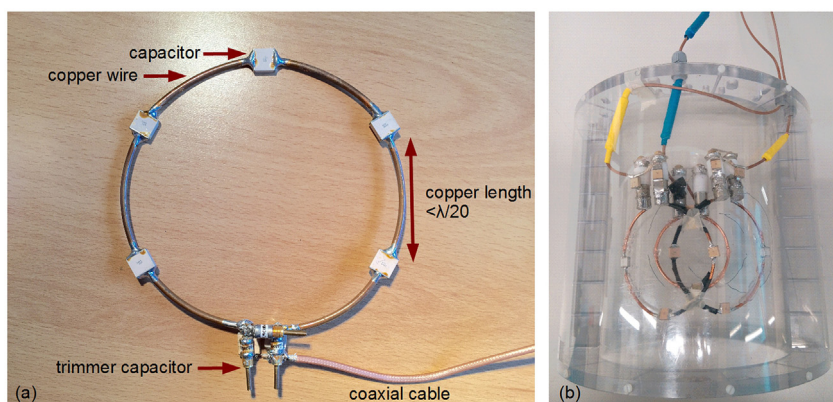


Fig. 1. (a) Picture of a loop RF coil consisting of five parallel-plate ceramic capacitors, copper wire, ceramic trimmer capacitors and a coaxial cable. As indicated in the picture, the length of the copper wire between two adjacent capacitors is less than $\lambda/20$. (b) Picture of single phosphorous (³¹P) (diameter = 6 cm)/quadrature proton (¹H) (diameter = 8 cm) loop coils used for 7 T MRI/MRS of the occipital lobe of the human brain.

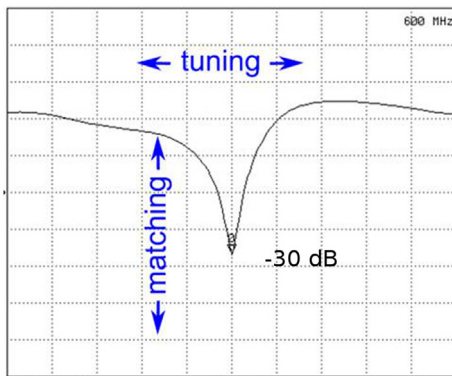


Fig. 2. Reflection coefficient (S11) measurement on a vector network analyzer (VNA). Here, the central frequency is set to 600 MHz with a 100 MHz span. The marker on the resonance peak shows -30 dB for the S11 coefficient at 600 MHz. The tuning of the peak changes by moving the peak through the various frequencies. On the other hand, the peak becomes smaller or bigger depending upon the matching.



Fig. 4. MR image of the human brain acquired at 7 Tesla. Circles represent regions in the image in which destructive interference of the MR signal occurs. Images were acquired by means of a 7 Tesla MR scanner (Siemens Magnetom, Erlangen) using a turbo echo spin echo sequence.

Advantages and challenges at ultra-high field MR

An increase in the static magnetic field offers various advantages for *in vivo* applications: an increase in signal-to-noise ratio (SNR) [8,9], higher spatial resolution [10], increased spectral resolution [11], increased sensitivity of the Blood-Oxygen-Level Dependent (BOLD) signals in the visualization of brain activity, an enhancement in T_2^* contrast [12] and higher parallel imaging performance [13,14].

On the other hand, an increase in the static magnetic fields brings about new physical challenges: decreased RF penetration in the subject under study, higher RF power requirements [15–17] and increased susceptibility and chemical shift artifacts [18]. Even more importantly, the RF wavelength in the body, which is inversely proportional to the frequency and the square root of the dielectric constant, becomes comparable to or smaller in size than the anatomical dimensions, which leads to signal voids and brightening [19]. While destructive interference leads to darkening of the image, constructive interference may lead to local brightening of the image (Fig. 4). Therefore, at ultra-high field MR imaging a strong contribution of the induced conductive and dielectric currents to RF-induced signal variations across the subject are highly visible. Compared to more conventional 3T MR systems, achievable B_1^+ (transmit) fields are also limited by less powerful RF power amplifiers (2×15 kW at 3T, compared to 2×4 kW or a few installations of 16×1 kW at 7T) and inherently higher cable losses leading to increased signal attenuation. This results in a situation in which RF-power-demanding sequences,

such as spin echo applied to large cross-sections, face challenges with respect to sufficiently available B_1^+ and imaging speed due to increased RF-heating concerns.

The ultimate goal in increasing the main magnetic field strength is to achieve molecular-level high resolution to understand the brain structure and metabolism in greater detail than presently available. Currently, the sensitivity of available RF coils is limited for microscopic imaging without administration of a contrast agent to the subject. Molecular level imaging is possible only with the application of specialized molecular sensors. For example, combining dopamine imaging with functional MRI (fMRI) techniques allows for a better understanding of how dopamine levels influence neural circuitry [20].

RF coils at ultra-high field MR

The quadrature birdcage coil is the “workhorse” transmit coil at lower field strengths. Various versions of volume quadrature coils have been adapted for use in ultra-high field head and abdomen imaging of human subjects. For head imaging, despite the fact that a 7 T birdcage coil can still achieve reasonable B_1^+ levels, signal homogeneity is an issue due to image brightening in the center of

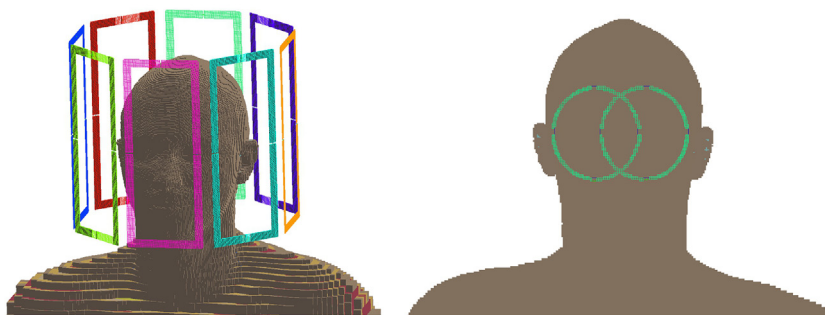


Fig. 3. Schematic of (left) a volume coil consisting of eight rectangular loops encircling the human head, and (right) surface coils consisting of two circular loop coils placed just behind the occipital lobe of the human brain. These schematics were modeled and voxelized by means of the Sim4Life simulation package (ZMT, Zurich, Switzerland). Interested readers may wish to consult <https://www.zurichmedtech.com/sim4life>.

the field of view. Moreover, for abdomen imaging, a 7T volume coil shows limited RF penetration and elevated RF heating in the subject's head, a region outside the RF coil [21]. Recently, Orzada et al. [22] presented a whole-body 32-channel microstrip array, but they were confronted with the issue of limited RF penetration into the body even when maximizing RF power input by placing the RF power amplifiers next to the magnet. This is still preliminary, ongoing hardware development.

Understanding the coil/subject interaction is crucial for obtaining a homogeneous image. The subject, with its various air-, fluid- and tissue-filled cavities, presents a heterogeneous dielectric load, which leads to refraction and reflection of the field components at the tissue boundaries, resulting in strong field interferences. Therefore, the field yielded in the subject by an RF coil strongly depends on the exact distribution of dielectric properties in the subject. Furthermore, wave propagation effects destroy the ideal current distribution yielding inefficient transmit distribution on the RF coil around the subject, especially in conjunction with variable loading situations. One solution to this challenge may be the use of parallel-transmit methods. Multiple individual RF transmit coil array elements can be independently driven with various RF signal phases and amplitudes [23]. The RF field can be homogenized within the region of interest by shifting and manipulating signal void regions within the subject [24,25]. Moreover, user-defined shaped excitation for zoomed imaging is also used in functional MRI (fMRI). Imaging a specific region with a reduced FOV enables faster imaging with reduced sensitivity to motion.

Safety assessment at ultra-high field

A major challenge at ultra-high field imaging is the potential for tissue heating. RF pulses from the coil create time-varying magnetic-field induced electric fields in the subject according to Maxwell's equations. In other words, the electric field induces currents in the subject, which, in the case of conductive tissues, leads to tissue heating. Also, direct electric fields from the RF coil, especially around lumped elements, may also lead to tissue heating. The specific absorption rate (SAR) is a measure of the rate at which energy is absorbed by the human body when exposed to an electromagnetic field. It is defined as the power absorbed per mass of tissue and has units of watts per kilogram (W/kg). SAR limits are defined by the International Electrotechnical Commission (IEC) standard [26].

The local SAR level cannot be measured directly; instead, it is calculated based on electromagnetic field numerical simulations

using discrete human body models. Maximum local SAR levels tend to be higher in heterogeneous human models with tissues such as muscle and fat than in homogeneous models for a given magnetic field strength (by a factor of 2 or 3) [27,28]. For the volume coils and body surface arrays, the local SAR depends on large anatomical features such as height, weight, shoulder length, formation of current loops, the subject's position relative to the coil and the subject's posture (e.g. supine, prone, lateral). For rather small local surface coils, on the other hand, subject geometry and posture can be discarded because these coils are only sensitive to the area just under the conductors. It has been shown that simplified body models with three tissue types leads to similar local SAR levels as in the fully segmented body model with many tissue varieties [29,30]. Virtual observation points (VOPs) allow a compression of the domain, selecting only points with maximum SAR [31]. VOP models include many discrete human body models with different positioning for a specific coil. In a single VOP set, various body sizes and positions with respect to the RF coil are combined and local SAR matrices are determined in this data set by applying a lossy compression algorithm with a specific SAR overestimation [32].

The validation of simulation results is crucial. The preferred choice is to compare quantitatively calculated and experimentally measured B_1^+ maps to those obtained for a homogeneous phantom. Furthermore, validation procedures may include a second comparison, for example, temperature mapping or direct measurements of the RF field with field probes. Especially in the simulation of RF coil arrays, coupling is an aspect difficult to include reliably and the simulated EM fields may differ from the experimental results. Therefore, use of co-simulation [33] may improve the computational burden. When using multiple transmit channels, increased degrees of freedom in the electric field distribution lead to a complex SAR estimation [34]. Therefore, it is wise to calculate the worst-case local SAR for a transmit coil array to keep the scan parameters within the safety limits [35,36].

In addition to limits on local SAR, the IEC has issued limits on permissible MRI-induced temperature increases in human subjects. Since increased tissue temperature correlates with tissue damage, a better understanding of the relationship between temperature and SAR is desired. The relationship between SAR and temperature increase, however, is complicated [37,38]. Temperature increase is greatly affected by tissue-dependent perfusion values. In body areas with high perfusion, a minimal temperature increase can be expected in spite of its high SAR level, while in areas of lower perfusion, temperature may increase even with relatively low SAR levels [39]. Thermal conduction and heat loss to the environment

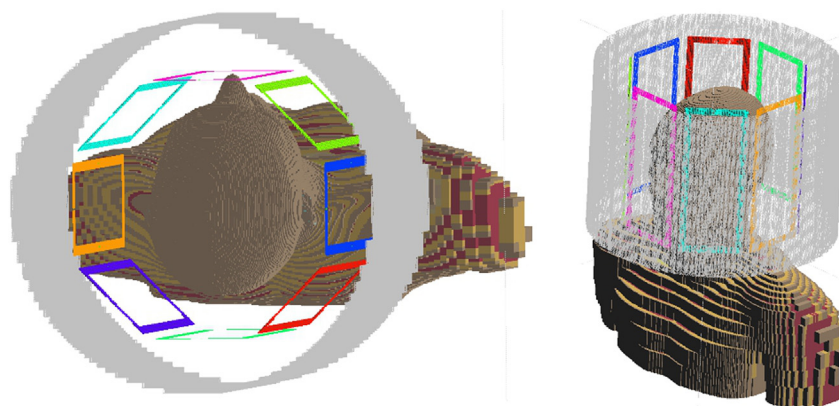


Fig. 5. Electromagnetic simulation model including the RF shield of the head-only gradient (gray), volume head RF coil (colored rectangles), Duke model from Virtual Population, IT'IS Foundation, Zurich, Switzerland; (left) top view and (right) lateral view. Interested readers may wish to consult <https://www.itis.ethz.ch/virtual-population/>.

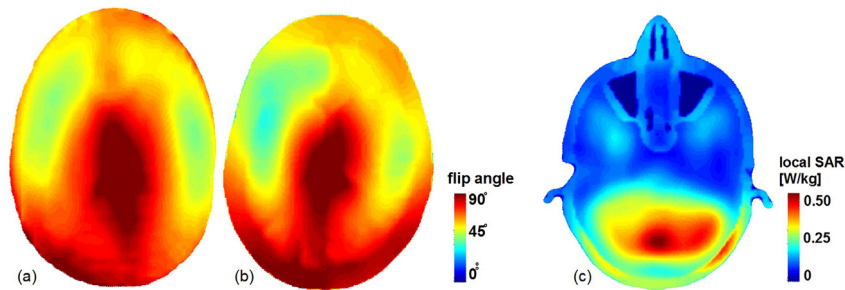


Fig. 6. (a) Measured and (b) simulated B_1^+ maps, and (c) simulated local SAR map for the human head (Duke from Virtual Population, IT'IS Foundation, Zurich, Switzerland) with the 7 T volume head coil (Nova Medical, Wilmington, MA). The B_1^+ map was acquired with a 7 Tesla MR scanner (Siemens Magnetom, Erlangen) and processed using Matlab software (Matworks Inc, Natick, MA).

also contribute to the dissimilarity between SAR and temperature distributions. Another thermal model using Cumulative Equivalent Minutes at 43 °C (CEM43) is proposed to estimate the tissue tolerances to the temperature rises in different durations and the suggested CEM43 threshold is sixteen minutes for skin, muscle, fat and bone heated during MR imaging [40].

Electromagnetic field (EM) simulations

Using Maxwell's equations, one can computationally model the electromagnetic interactions of an RF coil with its environment. An EM simulation starts with defining the model. A three-dimensional model of the magnet bore, subject (e.g. a human body [41] or a phantom) and RF coil can be created in a Computer-Aided Design (CAD) modeling environment (Fig. 5). First, a subject, whose dielectric properties determine the load on the RF coil, is chosen. Second, an RF coil, including an excitation port (typically a voltage source) and lumped elements (capacitors and inductors) is designed. The conductors of an RF coil are generally simulated as a Perfect Electric Conductor (PEC). Next, the whole model is discretized using mesh cells. The EM field across each mesh cell is then calculated. Numerical solvers using the Finite-difference Time-domain (FDTD) technique or the FEM/FIM (Finite Element/Integration Method) techniques give a direct solution to the Maxwell time-dependent curl equations [42]. Among these techniques, the FDTD method is essentially based on replacing the spatial and time-domain derivatives of Maxwell's equations with finite difference approximations [43]. Electric and magnetic field vector components are calculated on each Cartesian Yee cell. To create an FDTD model for MRI, an anatomically detailed human model (for the coil load) is needed as well as a coil grid [44]. The number of human body models available representing a realistic patient population is quite limited. A discrepancy between the SAR distribution in a patient and the simulated SAR results may appear when the patient anatomy differs significantly from that of the generic human model used to calculate the SAR. Furthermore, the validation of the simulation results is crucial, particularly in the simulation of RF coil arrays, because as, noted earlier, coupling is a difficult aspect to include reliably in simulations, and the simulated EM fields may differ from the experimental results. However, using subject-specific models [45,46] may improve the reliability of the simulations.

B_1^+ map (RF field mapping)

To determine the excitation field pattern, B_1^+ field mapping techniques are employed. This technique measures the effective flip angle in the region of interest for a certain pulse length. To measure the RF field map accurately, the image should be free of artifacts

due to B_0 inhomogeneity, incomplete longitudinal relaxation, slice (or slab) profiles, and cover a wide dynamic range of flip angles in the image without exceeding the SAR limits or having a long scan time [47]. Due to the existence of strong B_1^+ inhomogeneities, a B_1^+ mapping sequence with high dynamic range is an absolute requirement for ultra-high field MR. Unfortunately, a comparison of the ratio of signal intensities with incremented flip angles [48] or sequence timing [49] shows that there is a limited dynamic range in the region of interest, especially in deep tissue regions.

To map the RF-field distribution covering the depth region of a subject with an acceptable dynamic range, B_1^+ mapping techniques can be used. One such method consists of acquiring magnitude gradient echo images with several different flip angles and then determining the flip angles by fitting the signal intensity [50]. This method, however, is time consuming, SAR intensive and the relaxation time T_1 must be known beforehand. Hence, it is best suited for a homogeneous phantom. Another method is Bloch-Siegert B_1^+ mapping [51]. In this method, the Bloch-Siegert frequency shift is acquired as a phase image in the presence of off-resonance pulses. This phase shift is proportional to the square of the B_1^+ value. This method enables the correct determination of the B_1^+ value within a large dynamic range in a short time well below the SAR limits. Conversely, SA2RAGE (Saturation prepared with 2 Rapid Gradient Echoes) has been used to acquire the 3D B_1^+ map of a human brain accurately in under a minute with low SAR and low T_1 dependence [52]. DREAM (Dual Refocusing Echo Acquisition Method) is a recent method using magnetization-prepared FID and stimulated echo acquisition [53]. Because it is relaxation-free, it takes less than a minute to acquire two-dimensional B_1^+ maps with short repetition times or in three-dimensions (3DREAM) [54,55].

The validity of the SAR simulations can be verified with B_1^+ measurement. If the simulated and measured B_1^+ maps are comparable, the simulated SAR map is shown. An increase in the local SAR value occurs mainly with cerebrospinal fluid (CSF), skin and white matter for the 7 T head volume coil (Fig. 6c). Depending on the geometry and the excitation pattern of the RF coil, the maximum local SAR may either be located just under the RF coil conductors for the surface coils [56] or at the center of the brain for the volume coils (Fig. 6c).

Summary

Ultra-high field MR (>7 T) is advantageous for high resolution anatomic and functional imaging of the human body. However, ultra-high field strengths pose challenges of amplified signal inhomogeneities and increased heat deposition in tissues. Various RF coil designs have been explored here, including the basic theory of RF coils and their characterization steps. In addition, electromagnetic simulations, bench and MR measurements are described in

detail. A thorough evaluation of the parameters discussed herein will ensure that RF coils can be designed to obtain the best available image quality.

Acknowledgements

This study was supported by Centre d'Imagerie BioMédicale (CIBM) of the UNIL, UNIGE, HUG, CHUV, EPFL and the Leenaards and Jeantet Foundations. The author thanks to Dr. Hikari Yoshihara for his help in editing, Dr. Hongxia Lei for fruitful discussions and Jérémie Clément for his assistance in creating Fig. 6.

References

- [1] R.D.J.W.E. Doherty Jr., *The Pin Diode Circuit Designers Handbook*, Microsemi-watertown, 1998.
- [2] M.L.J. Mispelter, A. Briquet, *NMR Probeheads: for Biophysical and Biomedical Experiments*, Imperial college press, London, 2006.
- [3] D. Mager, A. Peter, L.D. Tin, E. Fischer, P.J. Smith, J. Hennig, J.G. Korvink, An MRI receiver coil produced by inkjet printing directly on to a flexible substrate, *IEEE Trans. Med. Imaging* 29 (2010) 482–487.
- [4] J.R. Corea, A.M. Flynn, B. Lechene, G. Scott, G.D. Reed, P.J. Shin, M. Lustig, A.C. Arias, Screen-printed flexible MRI receive coils, *Nat. Commun.* 7 (2016).
- [5] Q. Duan, J.H. Duyn, N. Gudino, J.A. de Zwart, P. van Gelderen, D.K. Sodickson, R. Brown, Characterization of a dielectric phantom for high-field magnetic resonance imaging applications, *Med. Phys.* 41 (2014) 102303.
- [6] J.R.G.J.T. Vaughan, *RF Coils for MRI*, John Wiley Sons, UK, 2012.
- [7] P.B. Roemer, W.A. Edelstein, C.E. Hayes, S.P. Souza, O.M. Mueller, The NMR phased array, *Magn. Reson. Med.* 16 (1990) 192–225.
- [8] D.I. Hoult, R.E. Richards, The signal-to-noise ratio of the nuclear magnetic resonance experiment, *J. Magn. Reson.* 213 (2011) 329–343.
- [9] J.T. Vaughan, M. Garwood, C.M. Collins, W. Liu, L. DelaBarre, G. Adriany, P. Andersen, H. Merkle, R. Goebel, M.B. Smith, K. Ugurbil, 7T vs. 4T: RF power, homogeneity, and signal-to-noise comparison in head images, *Magn. Reson. Med.* 46 (2001) 24–30.
- [10] E. Yacoub, A. Shmuel, J. Pfeuffer, P.-F. Van De Moortele, G. Adriany, P. Andersen, J.T. Vaughan, H. Merkle, K. Ugurbil, X. Hu, Imaging brain function in humans at 7 Tesla, *Magn. Reson. Med.* 45 (2001) 588–594.
- [11] R. Gruetter, S.A. Weisdorf, V. Rajanayagan, M. Terpstra, H. Merkle, C.L. Truitt, M. Garwood, S.L. Nyberg, K. Ugurbil, Resolution improvements in vivo 1H NMR spectra with increased magnetic field strength, *J. Magn. Reson.* 135 (1998) 260–264.
- [12] J.S. Gati, R.S. Menon, K. Ugurbil, B.K. Rutt, Experimental determination of the BOLD field strength dependence in vessels and tissue, *Magn. Reson. Med.* 38 (1997) 296–302.
- [13] K.P. Pruessmann, M. Weiger, M.B. Scheidegger, P. Boesiger, SENSE: sensitivity encoding for fast MRI, *Magn. Reson. Med.* 42 (1999) 592–596.
- [14] D.K. Sodickson, W.J. Manning, Simultaneous acquisition of spatial harmonics (SMASH): fast imaging with radiofrequency coil arrays, *Magn. Reson. Med.* 38 (1997) 591–603.
- [15] P.A. Bottomley, W.A. Edelstein, Power deposition in whole-body NMR imaging, *Med. Phys.* 8 (1981) 510–512.
- [16] C.N. Chen, V.J. Sank, S.M. Cohen, D.I. Hoult, The field dependence of NMR imaging. I. Laboratory assessment of signal-to-noise ratio and power deposition, *Magn. Reson. Med.* 3 (1986) 722–729.
- [17] D.I. Hoult, C.N. Chen, V.J. Sank, The field dependence of NMR imaging. II. Arguments concerning an optimal field strength, *Magn. Reson. Med.* 3 (1986) 730–746.
- [18] P.-M. Robitaille, L.J. Berliner, *Ultra High-field Magnetic Resonance Imaging*, Springer, New York, 2006.
- [19] C.M. Collins, W. Liu, W. Schreiber, Q.X. Yang, M.B. Smith, Central brightening due to constructive interference with, without, and despite dielectric resonance, *J. Magn. Reson. Imaging* 21 (2005) 192–196.
- [20] T. Lee, L.X. Cai, V.S. Lelyveld, A. Hai, A. Jasanoff, Molecular-level functional magnetic resonance imaging of dopaminergic signaling, *Science* 344 (2014) 533–535.
- [21] J.T. Vaughan, C.J. Snyder, L.J. DelaBarre, P.J. Bolan, J. Tian, L. Bolinger, G. Adriany, P. Andersen, J. Strupp, K. Ugurbil, Whole-body imaging at 7T: preliminary results, *Magn. Reson. Med.* 61 (2009) 244–248.
- [22] A.K.B.S. Orzada, O. Kraff, N. Oehmigen, M. Gratz, S. Johst, M.N. Volker, S.H.G. Rietsch, M. Floser, T. Fiedler, S. Shooshary, K. Solbach, H.H. Wuich, M.E. Ladd, A 32-channel integrated body coil for 7 Tesla whole-body imaging, *Proc. Int. Soc. Magn. Reson. Med.* (2016), 167.
- [23] C.M. Collins, W. Liu, B.J. Swift, M.B. Smith, Combination of optimized transmit arrays and some receive array reconstruction methods can yield homogeneous images at very high frequencies, *Magn. Reson. Med.* 54 (2005) 1327–1332.
- [24] G.J. Metzger, C. Snyder, C. Akgun, T. Vaughan, K. Ugurbil, P.F. Van de Moortele, Local B1+ shimming for prostate imaging with transmitter arrays at 7T based on subject-dependent transmit phase measurements, *Magn. Reson. Med.* 59 (2008) 396–409.
- [25] S. Orzada, S. Maderwald, B.A. Poser, A.K. Bitz, H.H. Quick, M.E. Ladd, RF excitation using time interleaved acquisition of modes (TIAMO) to address B1 inhomogeneity in high-field MRI, *Magn. Reson. Med.* 64 (2010) 327–333.
- [26] International electrotechnical commission, in: IEC (Ed.), *Medical Equipment - IEC 60601-2-33: Particular Requirements for the Safety of Magnetic Resonance Equipment*, 2010. Geneva.
- [27] C.M. Collins, Z. Wang, Calculation of radiofrequency electromagnetic fields and their effects in MRI of human subjects, *Magn. Reson. Med.* 65 (2011) 1470–1482.
- [28] S. Oh, A.G. Webb, T. Neuberger, B. Park, C.M. Collins, Experimental and numerical assessment of MRI-induced temperature change and SAR distributions in phantoms and in vivo, *Magn. Reson. Med.* 63 (2010) 218–223.
- [29] H. Homann, P. Börner, H. Eggers, K. Nehrke, O. Dössel, I. Graesslin, Toward individualized SAR models and in vivo validation, *Magn. Reson. Med.* 66 (2011) 1767–1776.
- [30] Ö. Ipek, A.J. Raaijmakers, J.J. Lagendijk, P.R. Luitjen, C.A.T. van den Berg, Intersubject local SAR variation for 7T prostate MR imaging with an eight-channel single-side adapted dipole antenna array, *Magn. Reson. Med.* 71 (2014) 1559–1567.
- [31] G. Eichfelder, M. Gebhardt, Local specific absorption rate control for parallel transmission by virtual observation points, *Magn. Reson. Med.* 66 (2011) 1468–1476.
- [32] A. Bitz, R. Gumbrecht, S. Orzada, H.-F. Fautz, M. Ladd, Evaluation of virtual observation points for local SAR monitoring of multi-channel transmit RF coils at 7 Tesla, *Proc. Int. Soc. Magn. Reson. Med.* (2013) 4414.
- [33] M. Kozlov, R. Turner, Fast MRI coil analysis based on 3-D electromagnetic and RF circuit co-simulation (San Diego, Calif. : 1997), *J. Magn. Reson.* 200 (2009) 147–152.
- [34] F. Seifert, G. Wubbeler, S. Junge, B. Ittermann, H. Rinneberg, Patient safety concept for multichannel transmit coils, *J. Magn. Reson. imaging* 26 (2007) 1315–1321.
- [35] M. de Greef, O. Ipek, A.J. Raaijmakers, J. Crezee, C.A. van den Berg, Specific absorption rate intersubject variability in 7T parallel transmit MRI of the head, *Magn. Reson. Med.* 69 (2013) 1476–1485.
- [36] Ö. Ipek, A.J. Raaijmakers, J.J. Lagendijk, P.R. Luitjen, C.A. van den Berg, Intersubject local SAR variation for 7T prostate MR imaging with an eight-channel single-side adapted dipole antenna array, *Magn. Reson. Med.* 71 (2014) 1559–1567.
- [37] E.N.M. Murbach, K.P. Pruessmann, N. Kuster, Safe MR scan times based on CEM43 tissue damage thresholds, using electromagnetic and thermal simulations with anatomically correct human models and considering local thermoregulation, *Proc. Int. Soc. Magn. Reson. Med.* (2012) 313.
- [38] Z. Wang, J.C. Lin, W. Mao, W. Liu, M.B. Smith, C.M. Collins, SAR and temperature: simulations and comparison to regulatory limits for MRI, *J. Magn. Reson. imaging* 26 (2007) 437–441.
- [39] C.M. Collins, W. Liu, J. Wang, R. Gruetter, J.T. Vaughan, K. Ugurbil, M.B. Smith, Temperature and SAR calculations for a human head within volume and surface coils at 64 and 300 MHz, *J. Magn. Reson. imaging* 19 (2004) 650–656.
- [40] G.C. van Rhoon, T. Samaras, P.S. Yarmolenko, M.W. Dewhirst, E. Neufeld, N. Kuster, CEM43 degrees C thermal dose thresholds: a potential guide for magnetic resonance radiofrequency exposure levels? *Eur. Radiol.* 23 (2013) 2215–2227.
- [41] A. Christ, W. Kainz, E.G. Hahn, K. Honegger, M. Zefferer, E. Neufeld, W. Rascher, R. Janka, W. Bautz, J. Chen, B. Kiefer, P. Schmitt, H.P. Hollenbach, J. Shen, M. Oberler, D. Szczerba, A. Kam, J.W. Guag, N. Kuster, The Virtual Family—development of surface-based anatomical models of two adults and two children for dosimetric simulations, *Phys. Med. Biol.* 55 (2010) N23–N38.
- [42] Y. Kane, Numerical solution of initial boundary value problems involving Maxwell's equations in isotropic media, *IEEE Trans. Antennas Propag.* 14 (1966) 302–307.
- [43] S.C.H.A. Taflov, *Computational Electrodynamics: the Finite Difference Time Domain Method*, Artech House, Boston, 2000.
- [44] T.S. Ibrahim, R. Lee, B.A. Baertlein, A. Kangarlu, P.L. Robitaille, Application of finite difference time domain method for the design of birdcage RF head coils using multi-port excitations, *Magn. Reson. imaging* 18 (2000) 733–742.
- [45] H. Homann, P. Bornert, H. Eggers, K. Nehrke, O. Dössel, I. Graesslin, Toward individualized SAR models and in vivo validation, *Magn. Reson. Med.* 66 (2011) 1767–1776.
- [46] J. Jin, F. Liu, E. Weber, S. Crozier, Improving SAR estimations in MRI using subject-specific models, *Phys. Med. Biol.* 57 (2012) 8153–8171.
- [47] N.G. Dowell, P.S. Tofts, Fast, accurate, and precise mapping of the RF field in vivo using the 180 degrees signal null, *Magn. Reson. Med.* 58 (2007) 622–630.
- [48] V.L. Yarnykh, Actual flip-angle imaging in the pulsed steady state: a method for rapid three-dimensional mapping of the transmitted radiofrequency field, *Magn. Reson. Med.* 57 (2007) 192–200.
- [49] C.H. Cunningham, J.M. Pauly, K.S. Nayak, Saturated double-angle method for rapid B1+ mapping, *Magn. Reson. Med.* 55 (2006) 1326–1333.
- [50] G.J. Barker, A. Simmons, S.R. Arridge, P.S. Tofts, A simple method for investigating the effects of non-uniformity of radiofrequency transmission and radiofrequency reception in MRI, *Br. J. Radiol.* 71 (1998) 59–67.
- [51] L.I. Sacolick, F. Wiesinger, I. Hancu, M.W. Vogel, B1 mapping by Bloch-Siegert shift, *Magn. Reson. Med.* 63 (2010) 1315–1322.
- [52] F. Eggenschwiler, T. Kober, A.W. Magill, R. Gruetter, J.P. Marques, SA2RAGE: a

- new sequence for fast B1+-mapping, *Magn. Reson. Med.* 67 (2012) 1609–1619.
- [53] K. Nehrke, P. Börnert, DREAM—a novel approach for robust, ultrafast, multi-slice B1 mapping, *Magn. Reson. Med.* 68 (2012) 1517–1526.
- [54] D. Brenner, D.H.Y. Tse, P.J. Ledden, C. Neumann, T. Stocker, Rapid and accurate pTx B1 mapping using 3DREAM with dual interferometry, *Proc. Int. Soc. Magn. Reson. Med.* (2015) 109.
- [55] D. Brenner, D.H.Y. Tse, E.D. Pracht, T. Feiweier, S.R., T. Stocker, 3DREAM - a three-dimensional variant of the DREAM sequence, *Proc. Int. Soc. Magn. Reson. Med.* (2014) 1455.
- [56] O. Ipek, A.J. Raaijmakers, D.W. Klomp, J.J. Lagendijk, P.R. Luijten, C.A. van den Berg, Characterization of transceive surface element designs for 7 tesla magnetic resonance imaging of the prostate: radiative antenna and micro-strip, *Phys. Med. Biol.* 57 (2012) 343–355.